Modeling Gas-Solids Entrainment into a Horizontal Gas Jet Submerged within a Fluidized Bed

Craig Hulet[1], Cedric Briens[1], Franco Berruti[1], Edward W. Chan[2]
[1]The University of Western Ontario
London ON Canada

[2]Syncrude Canada Ltd
Edmonton AB Canada

Introduction

Fluidized beds are employed in a multitude of processes whether they are catalytic or noncatalytic in nature, including fluid catalytic cracking (FCC), polymerization, drying, and agglomeration, to name but a few. One further example of the use of the fluidized bed is the upgrading of heavy oil and hydrocarbon residues using a fluid coker. About 15 – 20% of crude oil in Canada is processed in fluid cokers. The process of fluid coking involves injecting a heavy hydrocarbon feedstock, atomized with steam, into a fluidized bed of hot coke particles. The action of the resulting jet entrains the surrounding fluidized bed particles into the jet. The heavy oil molecules are then thermally cracked after depositing on the hot surface of the solid particles, yielding such valuable products as gasoline, kerosene, diesel fuel, and various petrochemical feedstocks. Good conversion and high yields are very dependent on the jet-bed interaction (i.e. achieving good dispersion of the liquid droplets onto the solid coke particles that are entrained into the jet) (House et al., 2004). One of the key elements in achieving greater dispersion is the entrainment of the fluidized solids into the jet. In other words, the greater the number of hot coke particles with which the liquid droplets come into contact, and the more evenly dispersed the liquid is, both between and on the surface of these particles, the better the yield. Good dispersion and mixing also reduce sulphur and carbon dioxide emissions by allowing operation at lower reactor temperatures. Recently, the enhanced solids entrainment (ESE) device was proposed as a means to improve mixing between gas-liquid jets and the entrained solid coke particles (Chan et al., 2006; House et al., 2004). ESE is comprised of a cylindrical draft tube mounted coaxially downstream of the horizontally aligned spray nozzle (see Figure 1). Felli (2002) developed and a validated a novel technique for measuring the entrainment of fluidized solids into a horizontal jet submerged within a fluidized bed. This body of work was continued and extended by Hulet et al. (2003).

Recently, Hulet et al. (2006a/b) demonstrated the effectiveness of a shroud installed at the end of the nozzle in increasing the solids entrainment rate into the draft tube located downstream (a typical shroud is illustrated in Figure 2). The objective of this study was to model the gas-particle interaction phenomena between the nozzle and draft tube and to investigate how it was altered by the presence of the shroud. The CFD software FLUENT (version 6.2.16) was used for this study. CFD has been applied to many gas-particle systems in recent years. Of course, the majority of the reported work concentrates on the hydrodynamics of fluidization and report on the performance of CFD and comparing the simulation results to those found in the lab. Taghipour et al. (2003) studied the bed expansion ratio and pressure drop. A large body of work has been published by van Wachem and his colleagues on the modeling of fluidized beds including work on the pressure fluctuations (van Wachem et al., 1999) and bubbling (van Wachem et al., 1998) in fluidized beds. Finally van Wachem et al. (2001) provide a thorough review of the various CFD models currently in use.
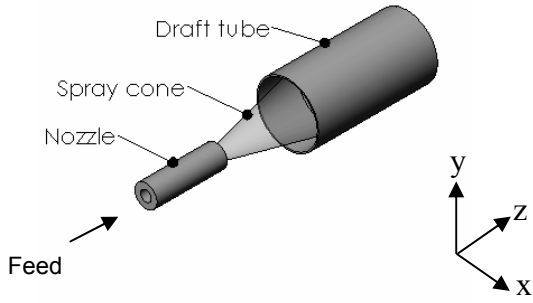
Figure 1. Isometric view of nozzle and draft tube arrangement.
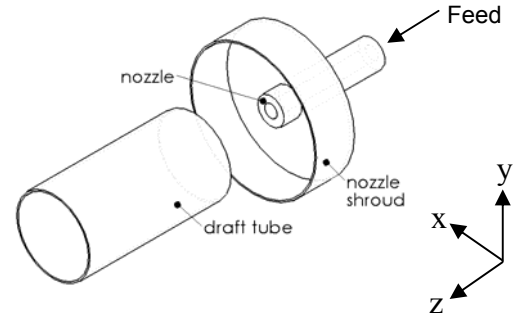
Figure 2. Illustration of a typical nozzle shroud arrangement.

Very little literature was found on the CFD modeling of submerged gas jets in fluidized beds. Zhang et al. (2004) studied the voidage profile and jet penetration of a gas jet in a fluidized bed, while Tyler and Mees (1999) have examined the hydrodynamics of a horizontally submerged jet in a fluidized bed. Simulations have been performed using spouted fluidized beds in order to study the effects of the frictional stress, maximum packing limit and coefficient of restitution on the voidage and velocity profiles of the gas and solid phases (Du et al., 2006a). Du et al. (2006b) also studied the effect of the drag coefficient correlation and demonstrated its significant impact on the flow patterns and voidage distribution in the simulations they conducted especially if the particles are prone to clustering. However, there is still no consensus as to the choice of which drag force model to use (Kandhai et al., 2003; Yang et al., 2003). Makkawi and Ocone (2005) provide a review and evaluation on the aspects of modeling the particle stress covering the entire range of flow regimes, and their main conclusion is again that no one model clearly outperforms the other and that more experimental and theoretical work is required.

Theoretical Background

Governing Equations

Conservation of Mass

The general form of the continuity equation for phase i is given by Equation 1 (assuming zero mass transfer between phases):

$$\frac{\partial}{\partial t}\left(\alpha_q \rho_q\right) + \nabla \cdot \left(\alpha_q \rho_q \vec{v}_q\right) = 0 \tag{1}$$

by definition, the phase volume fractions $\sum \alpha_q = 1$.

Conservation of Momentum

The general form for the momentum balance equation for phase i is shown as Equation 2:

$$\frac{\partial}{\partial t}\left(\alpha_q \rho_q \vec{v}_q\right) + \nabla \cdot \left(\alpha_q \rho_q \vec{v}_q \vec{v}_q\right) = -\alpha_q \nabla P + \alpha_q \rho_q g + \nabla \cdot \overline{\overline{\tau}}_q + \sum_{p=1}^{n} \vec{R}_{pq} + \vec{F}_q \tag{2}$$

where $\vec{F}_q$ represents any external body force, $\vec{R}_{pq}$ is the interaction force between phases and P is the shared pressure. For the ith phase with shear and bulk viscosity μ_q and λ_q, respectively, the Reynolds stress tensor is given by Equation 3:

$$\overline{\overline{\tau}}_q = \alpha_q \mu_q \left(\nabla \vec{v}_q + \nabla \vec{v}_q^T \right) + \alpha_q \left(\lambda_q - \frac{2}{3} \mu_q \right) \nabla \cdot \vec{v}_q \overline{\overline{I}} \tag{3}$$

For the gas phase, Equation 3 becomes:

$$\overline{\overline{\tau}}_g = \mu_{g,e} \left[\left(\frac{\partial u_i}{\partial x_j} + \frac{\partial u_j}{\partial x_i} \right) - \frac{2}{3} \delta_{ij} \frac{\partial u_k}{\partial x_k} \right] \tag{4}$$

where $\mu_{g,e}$ is the effective turbulent viscosity given by the summation of the laminar viscosity $\mu_{g,l}$ and the turbulent viscosity $\mu_{g,T}$ as given by Equation 5:

$$\mu_{g,T} = \alpha_g \rho_g C_\mu \frac{\kappa_g^2}{\varepsilon_g} \tag{5}$$

In Equation 5, C_μ is an empirical constant, κ_g represents the turbulent kinetic energy, and ε_g its turbulent dissipation rate. The latter two parameters must be obtained using a given turbulence model. Similarly, the Reynolds stress tensor for the solids phase is given below:

$$\overline{\overline{\tau}}_s = -P_s \delta_{ij} + \alpha_s \lambda_s \delta_{ij} \frac{\partial u_i}{\partial x_i} + \alpha_s \mu_s \left[\left(\frac{\partial u_j}{\partial x_i} + \frac{\partial u_i}{\partial x_j} \right) - \frac{2}{3} \delta_{ij} \frac{\partial u_k}{\partial x_k} \right] \tag{6}$$

Here, the solids bulk viscosity λ_s represents the resistance of the particulate phase to compression and expansion forces: it is obtained using the form attributed to Lun et al. (1984):

$$\lambda_s = \frac{4}{3} \alpha_s \rho_s d_p g_{0,ss} \left(1 + e_{ss} \right) \left(\frac{\Theta_s}{\pi} \right)^{0.5} \tag{7}$$

The shear viscosity, μ_s, arises from the particle momentum exchanged due to translation and collisions and consists of two parts: a collisional component $\mu_{s,col}$ and a kinetic component $\mu_{s,kin}$ (Syamlal et al., 1993):

$$\mu_{s,col} = \frac{4}{5} \alpha_s \rho_s d_p g_{0,ss} \left(1 + e_{ss} \right) \left(\frac{\Theta_s}{\pi} \right)^{0.5} \tag{8}$$

$$\mu_{s,kin} = \frac{\alpha_s d_p \rho_s \sqrt{\Theta_s \pi}}{6 \left(3 - e_{ss} \right)} \left[1 + \frac{2}{5} \left(1 + e_{ss} \right) \left(3 e_{ss} - 1 \right) \alpha_s g_{0,ss} \right] \tag{9}$$

The solids pressure is calculated independently and used in the pressure gradient term ∇P_s in the granular phase momentum equation when the granular flow is in the "compressible" regime (i.e. the solids volume fraction is less than the maximum packing limit). The solids pressure is determined using Equation 10:

$$P_s = \alpha_s \rho_s \Theta_s + 2 \rho_s \left(1 + e_{ss} \right) \alpha_s^2 g_{0,ss} \Theta_s \tag{10}$$

where e_{ss} is the restitution coefficient of particle-particle collisions, $g_{0,ss}$ is the radial distribution function, and Θ_s is the granular temperature. In general, the coefficient of restitution affects how much momentum the particle looses during a collision, which will affect the overall turbulence of the particulate phase. The granular temperature is proportional to the kinetic energy of the fluctuating particle motion while the distribution function modifies the probability of collisions between particles when the flow regime transitions from "compressible" (i.e. dilute) to "incompressible" (i.e dense). Compressible flow occurs when $\alpha_s < \alpha_{s,max}$ (i.e. the maximum packing limit) and continues until $\alpha_s = \alpha_{s,max}$ after which the particle spacing is maintained constant. It is also interpreted as a non-dimensional distance between the particles. The expression used in this study is from Ogawa et al. (1980):

$$g_{0,ss} = \left[1 - \left(\frac{\alpha_s}{\alpha_{s,max}} \right)^{1/3} \right]^{-1} \tag{11}$$

Finally, the granular temperature is given by Ding and Gidaspow (1990) in Equation 12:

$$\frac{3}{2}\left[\frac{\partial}{\partial t}(\rho_s \alpha_s \Theta_s) + \nabla \cdot (\rho_s \alpha_s \vec{v}_s \Theta_s) \right] = \left(-P_s \overline{\overline{I}} + \overline{\overline{\tau}}_s \right) : \nabla \vec{v}_s + \nabla \cdot \left(\kappa_{\Theta_s} \nabla \Theta_s \right) - \gamma \Theta_s + \phi_{ls} \tag{12}$$

where $\left(-P_s \overline{\overline{I}} + \overline{\overline{\tau}}_s \right) : \nabla \vec{v}_s$ represents the energy generated by the solid stress tensor, $\kappa_{\Theta_s} \nabla \Theta_s$ represents the diffusive flux of granular energy (see Equation 13), $\gamma \Theta_s$ represents the dissipation of energy due to collisions (see Equation 14), and ϕ_{ls} represents the energy exchanged between the lth fluid phase and the sth solid phase (see Equation 15):

$$\kappa_{\Theta_s} = \frac{15 d_p \rho_s \alpha_s \sqrt{\Theta_s \pi}}{4(41 - 33\eta)} \left[1 + \frac{12}{5}\eta^2 (4\eta - 3)\alpha_s g_{0,ss} + \frac{16}{15\pi}(41 - 33\eta)\eta \alpha_s g_{0,ss} \right] \tag{13}$$

with $\eta = 0.5(1 + e_{ss})$,

$$\gamma \Theta_m = \frac{12(1 - e_{ss}^2) g_{0,ss}}{d_p \sqrt{\pi}} \rho_s \alpha_s \Theta_s^{3/2} \tag{14}$$

$$\phi_{ls} = -3K_{sg}\Theta_s \tag{15}$$

Interphase Exchange Coefficients

One of the dominant forces in fluidized beds is the drag force exerted by the gas on the particulate phase. The general form for this interaction term is represented by Equation 16:

$$\sum_{j=1}^{n} \vec{R}_{pq} = \sum_{p=1}^{n} K_{pq} \left(\vec{v}_p - \vec{v}_q \right) \tag{16}$$

The fluid-solid drag force model selected for the closure expression is attributed to Syamlal-O'Brien (1985). It is based on the particle terminal velocity as measured in fluidized or settling beds. The correlations are a function of the volume fraction and the slip Reynolds number. The general form is given by Equation 17:

$$K_{sg} = \frac{\alpha_s \rho_s f}{\tau_s} \tag{17}$$

where f is defined according to the selected drag force model and τ_s is the particle relaxation time defined according to Equation 18.

$$\tau_s = \frac{\rho_s d_p^2}{18\mu_g} \tag{18}$$

For the Syamlal-O'Brien drag force model f is defined by Equation 19:

$$f = \frac{C_D N_{Re\,p} \alpha_g}{24 v_{r,s}^2} \tag{19}$$

where N_{Rep} is the particle Reynolds number based on the slip velocity given by Equation 20, C_D is the drag function based on the form given by DallaValle (1948) in Equation 21, and $v_{r,s}$ is the terminal velocity correlation for the particulate phase given by Equation 22:

$$N_{Re\,p} = \frac{\rho_g d_p |\vec{v}_s - \vec{v}_g|}{\mu_g} \tag{20}$$

$$C_D = \left(0.63 + \frac{4.8}{\sqrt{N_{\mathrm{Re}\,p}/v_{r,s}}} \right)^2 \tag{21}$$

$$v_{r,s} = 0.5 \left(A - 0.06 N_{\mathrm{Re}\,p} + \sqrt{\left(0.06 N_{\mathrm{Re}\,p} \right)^2 + 0.12 N_{\mathrm{Re}\,p} \left(2B - A \right) + A^2} \right) \tag{22}$$

The coefficients A and B for Equation 22 are given by Equations 23 and 24, respectively:

$$A = \alpha_g^{4.14} \tag{23}$$

$$B = \begin{cases} P' \alpha_g^{4.14} & \alpha_g \leq 0.85 \\ \alpha_g^Q & \alpha_g > 0.85 \end{cases} \tag{24}$$

The default values for P' and Q are 0.8 and 2.65, respectively. However, after comparison to one experimental value for the solids entrainment rate into the draft tube F_s, these values were modified to match the fluidization characteristics of the given particles following the explanation of Zimmermann and Taghipour (2005) and Syamlal and O'Brien (2003). The values obtained for P' and Q were 1.030 and 1.095, respectively

Closure Relationships

The Standard κ-ε model
      The standard κ-ε model is semi-empirical, robust, and reasonably accurate, but can be over-diffusive in some situations. Of all the κ-ε variants, it requires the least amount of computational (CPU) time. Its derivation assumes that the flow is completely turbulent and that the effects of molecular viscosity are negligible. The κ and ε terms are obtained according to Equations 25 and 26, respectively:

$$\frac{\partial}{\partial t}(\rho \kappa) + \frac{\partial}{\partial x_i}(\rho \kappa u_i) = \frac{\partial}{\partial x_j}\left[\left(\mu + \frac{\mu_t}{\sigma_k} \right) \frac{\partial \kappa}{\partial x_j} \right] + G_\kappa - \rho \varepsilon \tag{25}$$

$$\frac{\partial}{\partial t}(\rho \varepsilon) + \frac{\partial}{\partial x_i}(\rho \varepsilon u_i) = \frac{\partial}{\partial x_j}\left[\left(\mu + \frac{\mu_t}{\sigma_\varepsilon} \right) \frac{\partial \varepsilon}{\partial x_j} \right] + C_{1\varepsilon} \frac{\varepsilon}{\kappa} G_\kappa - C_{2\varepsilon} \rho \frac{\varepsilon^2}{\kappa} \tag{26}$$

where G_κ is the generation term for the turbulence kinetic energy due to the mean velocity gradients. The turbulent viscosity is then determined in relation to κ and ε as given in Equation 27:

$$\mu_t = \rho C_\mu \frac{\kappa^2}{\varepsilon} \tag{27}$$

The values of the constants $C_{1\varepsilon}$, $C_{2\varepsilon}$, C_μ, σ_κ, and σ_ε for the above set of equations are 1.44, 1.92, 0.09, 1.0, and 1.3, respectively (FLUENT User Guide, 2005).

The RNG κ-ε model
      The RNG κ-ε model was derived using a statistical technique based on "renormalization group theory" but the equations have a similar form to those of the standard κ-ε model. The RNG κ-ε model is reportedly more accurate and applicable to a wider range of flows – a number of which are mentioned by Tu and Fletcher (1995); however, this model requires the more CPU time. Furthermore, it may be more susceptible to instabilities in the calculations because the turbulent viscosity is reduced in response to high rates of strain

(FLUENT User Guide, 2005). The transport equations for the RNG κ-ε model are given as Equations 28 and 29:

$$\frac{\partial}{\partial t}(\rho\kappa) + \frac{\partial}{\partial x_i}(\rho\kappa u_i) = \frac{\partial}{\partial x_j}\left[\alpha_\kappa \mu_{eff} \frac{\partial \kappa}{\partial x_j}\right] + G_\kappa - \rho\varepsilon \tag{28}$$

$$\frac{\partial}{\partial t}(\rho\varepsilon) + \frac{\partial}{\partial x_i}(\rho\varepsilon u_i) = \frac{\partial}{\partial x_j}\left[\alpha_\varepsilon \mu_{eff} \frac{\partial \varepsilon}{\partial x_j}\right] + C_{1\varepsilon}\frac{\varepsilon}{\kappa}G_\kappa - C_{2\varepsilon}\rho\frac{\varepsilon^2}{\kappa} \tag{29}$$

where the effective viscosity is determined using the differential Equation 30

$$d\left(\frac{\rho^2\kappa}{\sqrt{\varepsilon\mu}}\right) = 1.72\frac{\hat{v}}{\sqrt{\hat{v}^2 - 1 + C_v}} \tag{30}$$

where $\hat{v} = \mu_{eff}/\mu$ and $C_v \cong 100$. The values of the RNG κ-ε model constants $C_{1\varepsilon}$, $C_{2\varepsilon}$, and C_μ are 1.42, 1.68, and 0.0845 (FLUENT User Guide, 2005).

Solution Procedure
        FLUENT utilizes the finite-volume method for the implicit discretization of the governing equations, which, in the case of a gas-solid two-phase flow, are solved sequentially. In this manner, the linearized set of algebraic equations for a given variable (pressure for example) is solved taking into account all cells simultaneously. Since the value of each variable is stored at the center of each control volume, or cell, face values are determined using an interpolation process known as upwinding. The required values for first-order accurate schemes are determined by simply taking the cell centre value as the average of the entire cell. Such schemes yield better convergence but are subject to numerical diffusion. Second-order schemes like the QUICK scheme (FLUENT User Guide, 2005) are more accurate. Second-order upwinding involves the use of Taylor series expansions of the cell-centered solution about the cell centroid.
        The optimal approach established for this study consisted of conducting a few hundred initial iterations using a first order discretization scheme and the standard κ-ε model before switching to the RNG κ-ε model and the QUICK discretization scheme. In both instances, the κ-ε transport equations were solved for each phase since the primary flow field affecting the motion of solids (i.e. the jet) is in the turbulent regime. Control of the rate of change of any variable was achieved using so-called under-relaxation factors. This approach provided the best convergence rate; otherwise, oscillations in the solution field tended to form (indicated by the fluctuating equation residuals). In all cases, the solution residuals decreased to the order of $1e^{-5}$ as mentioned above.

Modeling

Computational Domain and Operating Parameters
        Figure 3 shows the computational domain for the simulation of the ESE nozzle system. The 3D computational domain is composed of only a portion of the fluidized bed consisting of the nozzle, draft tube, the partition wall, and the front and rear walls of the fluidized bed. In order to reduce the size of the computational domain, and hence the computational requirements of the simulation, only a portion of the nozzle was included extending into the domain from the vertical plane (i.e. x = 0). For the purpose of the simulations this boundary face was designated as a wall to minimize the number of "open" boundaries required. This

arrangement allows a direct comparison to experimental results. Referring to Figure 4, which shows a vertical slice of the computational domain taken at x = 0. The length L^* (z-axis) of the computational domain is 0.114 m while the height H^* (y-axis) and the width W^* (x-axis) of the domain are both 0.102 m. A typical mesh generated is shown in Figure 5.
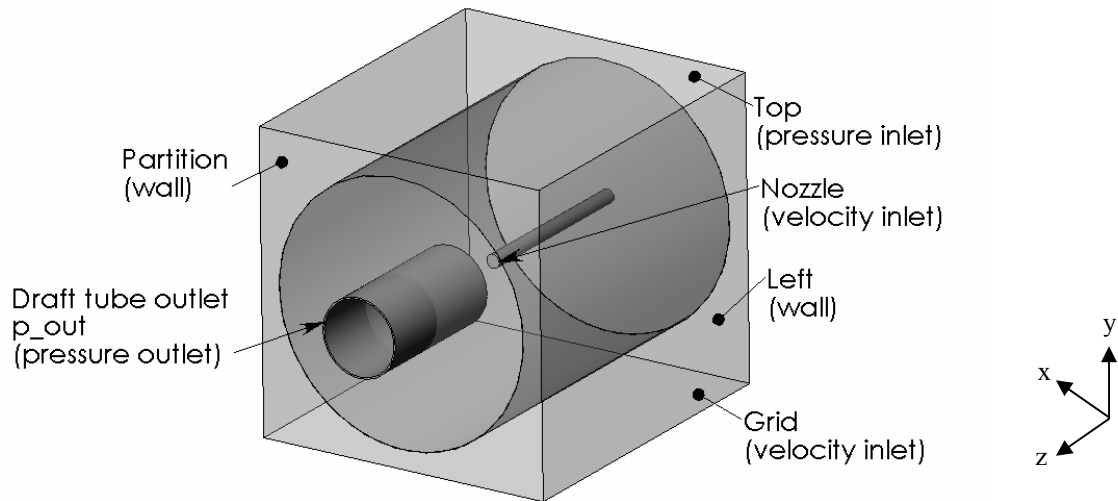
Figure 3. Illustration of the computational domain used for the CFD simulations.
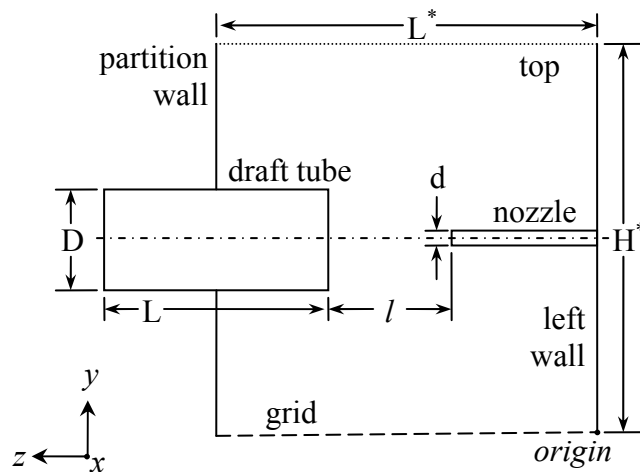
Figure 4. Illustration indicating the main geometric parameters of the CFD simulations.
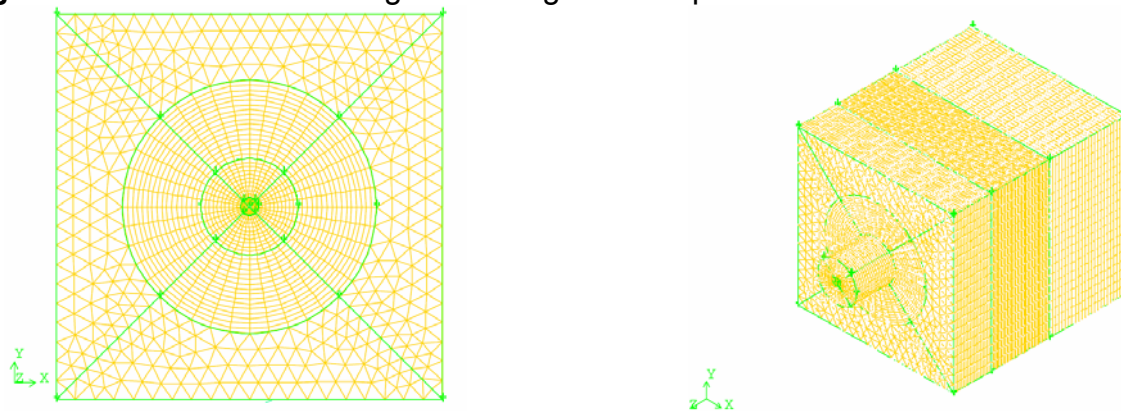
Figure 5. Typical mesh generated for a case without shroud (*l* = 0.038 m).

Table 1 summarizes the principle geometric and operational parameters considered in this study. For the purpose of this preliminary investigation the primary "variable" was the shroud. In total four cases were selected from the experimental study for simulation (for a fixed distance l comparison is made between the shrouded and non-shrouded results). The shrouded cases selected correspond to the experimental results that demonstrated the most significant increase in the measured solids entrainment rate (F_s). The particles used in the simulations were based on the same particles that were used in the experimental study (d_p = 135 μm) with the notable exception of the particle size distribution, which was assumed monosize. The particle and air densities were assumed constant at 1400 kg/m^3 and 1.225 kg/m^3, respectively.

Table 1. Geometric and operational parameters.

Variable	Value(s)	Units	Description
d	0.0045	m	Nozzle diameter
l	0.025/0.038	m	Distance from nozzle tip to draft tube inlet
D	0.025	m	Draft tube diameter
L	0.051	m	Draft tube length
F_g	0.00075	kg/s	Gas mass flow rate leaving nozzle tip (Nominal velocity = 162 m/s)

Simulation Settings

All simulations were conducted using the double precision segregated solver and a Eulerian-Eulerian description of both phases. The RNG κ-ε model and the QUICK discretization scheme was employed for the every simulation (after using the standard κ-ε model and a first-order discretization scheme for the first few hundred iterations, as recommended in the FLUENT User Manual, 2005). All default values for both the standard and RNG κ-ε models were retained with the exception of $C_{1\varepsilon}$, which was set to 1.56 as recommended by Cui et al. (2005). The operating pressure was set to 101325 Pa and the effect of gravity was included. The Syamlal drag force model was modified by means of a user defined function (UDF) as described above.

Boundary and Initial Conditions

The boundary conditions for the gas and solid phases are specified in Table 2. It is important to note that the pressure boundary for the draft tube outlet (p_out) is defined using a hydrostatic profile that would mimic the pressure distribution found in the experimental fluidized bed. This pressure profile is set with a user-defined function. Similarly, the static pressure at the "top" pressure inlet boundary is set to the value specified in order to mimic an overall fluidized bed height of 1.27 m.

It is assumed that there is zero penetration and zero accumulation at the walls. All remaining settings are left at their default values as given by FLUENT. The turbulence intensity was selected based on the work from Cui (2005). Since the nozzle orifice is round, the nozzle hydraulic diameter is simply equal to its outlet diameter. For the fluidized bed, the length scale was taken as 0.07 times the hydraulic diameter (where D_H is determined according to Equation 31):

$$D_H = \frac{4L^*W^*}{2\left(L^* + W^*\right)} \tag{31}$$

Table 2. Gas and solid phase boundary conditions.		
	Gas	*Solids*
Nozzle inlet & Grid		
Name	v_inlet & grid	
Type	velocity inlet	
Direction specification	z-axis & y-axis	
Value (m/s)	162 & 0.11	
Intensity (%)	5	
Length Scale (m)	0.0045 & $0.07H_D$	
Granular temperature (m^2/s^2)	n/a	0.0001
Volume fraction	1	0
Draft tube outlet & Free surface		
Name	p_out & top	
Type (pressure)	outlet & inlet	
Intensity (%)	5	
Length scale	$0.05D$ & $0.07H_D$	
Backflow granular temperature (m^2/s^2)	n/a	0.0001
Backflow volume fraction	0.44	0.56
Static Pressure (Pa)	$g\alpha_s(\rho_s - \rho_g)(H_{bed} - y)$ & 8978	

The solution was initialized by averaging the boundary conditions from all zones. For an *l* distance of 0.0381 m, it proved necessary to "patch" an initial small, non-zero gas velocity to the cylindrical volume within the draft tube in order to prevent solids from depositing and plugging the draft tube before the flow field could be established.

Solution Settings

As stated above, the flow, volume fraction, and the turbulence equations were solved by FLUENT using the phase-coupled SIMPLE approach. The under relaxation factors were modified and are summarized in Table 3. The under-relaxation factors were determined by trial and error to stabilize the flow and provide the best rate of convergence for the given simulations. In regards to the convergence criteria, it should be emphasized that, although the limits were set relatively high (i.e. 1×10^{-3}), the actual residuals fell well below this value (i.e. to the order of 1×10^{-5}).

Table 3. Under relaxation factors used in all simulations.

	Actual	*Default*		*Actual*	*Default*
Pressure	0.5	0.3	Granular temperature	0.2	0.2
Density	0.7	1	Turbulence kinetic energy	0.2	0.8
Body forces	1	1	Turbulence dissipation rate	0.2	0.8
Momentum	0.2	0.7	Turbulent viscosity	0.5	1
Volume fraction	0.5	0.2			

Grid size independence was achieved by constructing three meshes (M1, M2, and M3) with approximately 90000, 160000, and 260000 mixed hexahedral and tetrahedral cells, respectively. Starting with the coarsest mesh (M1), the grid spacing was refined by 20% in order to create a finer mesh (Slater, 2006). As may be seen from Figure 5, the mesh distribution was concentrated in the region between the nozzle and the draft tube in both the axial and radial directions. The cell spacing in these regions was chosen so that the transition

rate between cells was always 20% or lower as recommended in the FLUENT User Guide (2005). The difference in the average calculated solids flow rate, F_s, exiting the draft tube was used for the convergence criteria. The difference in this value was less than 5% between meshes M1 and M2 and less than 3% between meshes M2 and M3. Based on these results, the mesh spacing from mesh M2 was retained and applied to all subsequent meshes. For the grid independence tests the time step size was maintained at $5e^{-3}$ s and the l distance at 0.025 m.

A similar approach was applied in determining the time step size independence. Three time step sizes ($\Delta T1$, $\Delta T2$, and $\Delta T3$) of 5×10^{-3} s, 1×10^{-3} s, and 1×10^{-4} s, respectively, were tested using grid spacing obtained from the grid independence study. The difference in the F_s value was greater than 5% between time step sizes $\Delta T1$ and $\Delta T2$ and was just under 5% between time step sizes $\Delta T2$ and $\Delta T3$. Based on these results, a time step size of $1e^{-5}$ s was selected and applied to all subsequent simulations. It should be noted that for simulations where $l = 0.038$ m, it proved necessary to reduce the time step size to 1×10^{-6} for the initial phase of the simulation in order to achieve good convergence.

Results and Discussions

Figure 6 provides a representative sample of the typical variation of F_s (i.e. solids mass flow rate exiting the draft tube) with respect to time for a case without shroud and $l = 0.025$ m. As may be seen from the graph, the solids entrainment rate "spikes" (i.e reaches a maximum value) early in the simulation as the flow field is not yet established. Then, after approximately 0.8 s of simulated time, the output reaches a quasi-steady state. The solids entrainment rates, which are summarized in Table 4, were determined for each simulation by taking the average value over the subsequent 1 to 2 s time period.
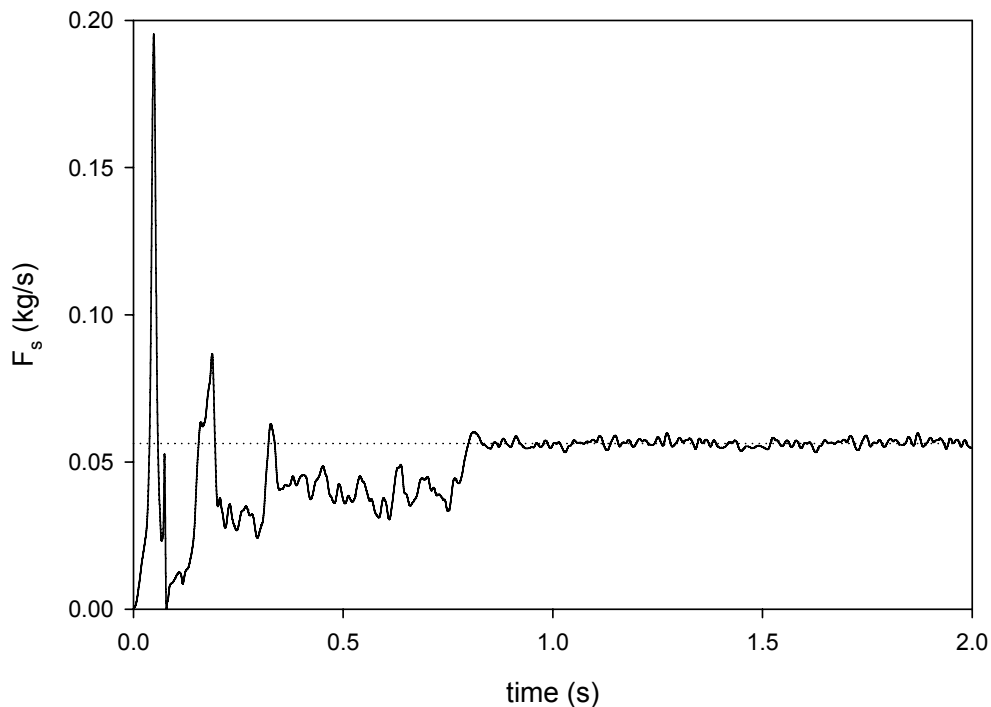
Figure 6. Solids entrainment versus time for the case $l = 0.025$ and without shroud.

Table 4. Summary of results for the four cases.

Case	Configuration	l (m)	Experimental F_s (kg/s)	Simulated F_s (kg/s)
1	shroud	0.025	0.051	0.056
2	no shroud	0.025	0.104	0.094
3	shroud	0.038	0.066	0.069
4	no shroud	0.038	0.103	0.091

Figures 7 through 18 graphs show the flow patterns for the gas and solid phases that were taken after approximately 1 s of simulated time had elapsed. For the "horizontal" planes the gravity vector points into the page and for the "vertical" planes the gravity vector points down towards the caption (the nozzle is always shown on the left, the draft tube on the right, and the grid on the bottom – see Figures 19 and 20). Figures 7 through 10 correspond to case 4 (without shroud, l = 0.038 m). Figure 7 and Figure 8 show the primary flow patterns – as uniformly sized velocity vectors of the axial velocity for the gas and solid phases, respectively – on a vertical slice through the computational domain at x = 0. Figure 9 and Figure 10 show a similar set of velocity vectors on the horizontal plane at y = 0.051 m (i.e. at the midsection of the computational domain). The same pattern is repeated for case 3 (with shroud, l = 0.038 m) in Figures 11 through 14. Finally, Figures 15 through 18 shows the solids holdup at the same instant in time as the figures described above. Figures 15 and 16 show the solids holdup on the vertical plane (x = 0) for case 3 and case 4, respectively. The solid holdups on the horizontal plane (y = 0.051) for the same cases are given in Figures 17 and 18. It is important to remark that the preponderance of arrows in the cylinder extending from the nozzle outlet through the draft tube is an artifact of the concentration of cells placed in this region (the vectors originate from each individual cell centre).

The most striking difference between the flow fields without and with shroud are the strong recirculation zones that are evident in Figure 11 (gas phase – vertical plane) above and below the jet and extending just past the mouth of the shroud. In Figure 13, (gas phase – horizontal plane) there is evidence of strong recirculation zone just in the immediate vicinity to either side of the nozzle tip. In contrast, there are only relatively small recirculation zones evident in Figure 12 (solid phase – vertical plane) and Figure 14 (solid phase – horizontal plane) located near the inside wall of the shroud. This is not unexpected given the relative densities of two phases and the relatively high particle relaxation time. These strong recirculation zones benefit the entrainment rate into the draft in two major ways. First, the strong recirculation zones would be areas of relatively low pressure which would act to enhance the entrainment towards the nozzle tip. Second, less gas would need to be entrained in order to entrain particles since a relatively large portion of the gas is "recycled" as it loops around and "shuttles" solids entering the shroud region to the nozzle tip before returning to the
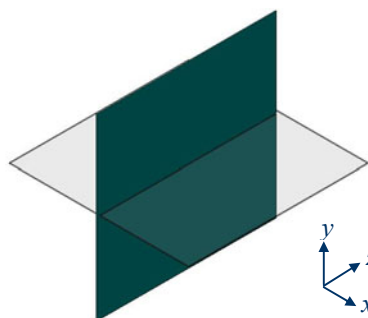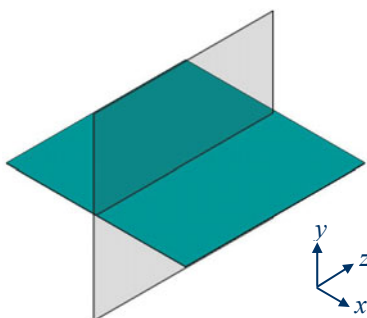
Figure 19: Horizontal plane.   Figure 20: Vertical plane.
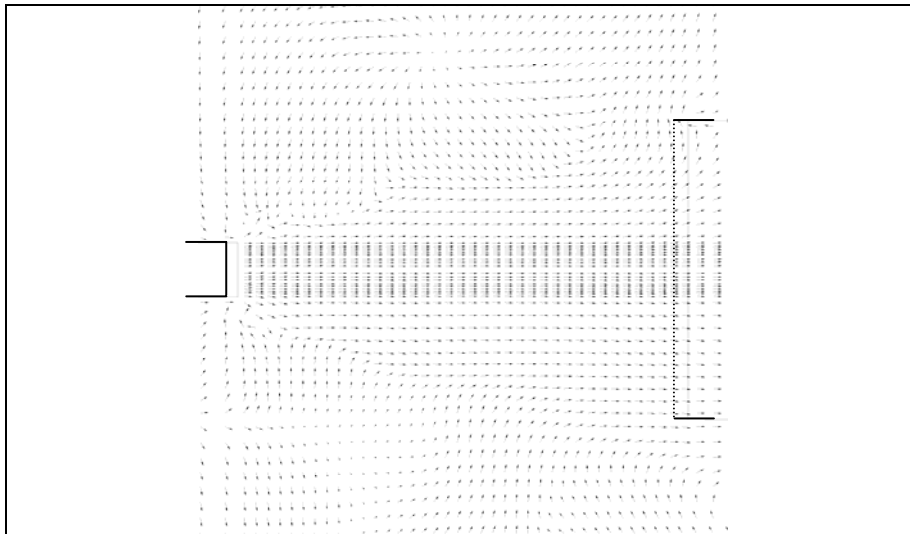
Figure 7. Flow field; no shroud; air; vertical plane.
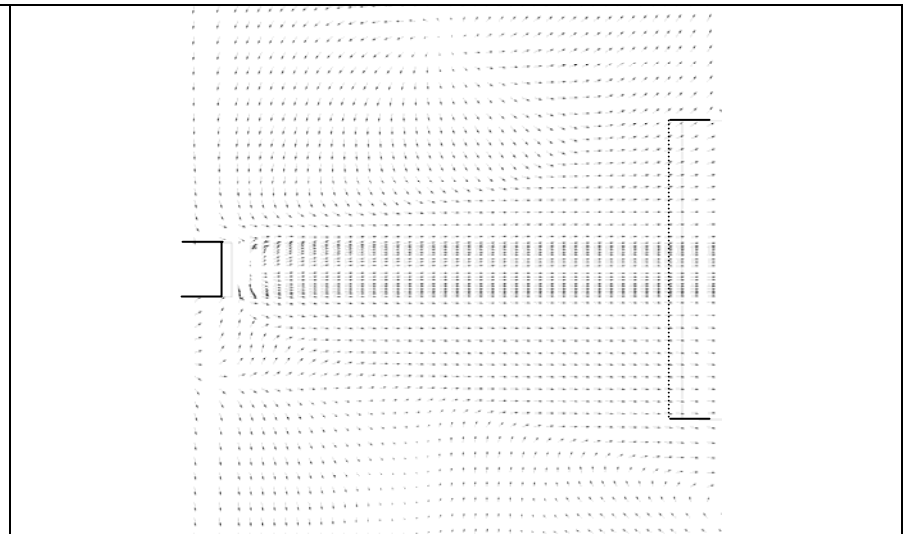
Figure 8. Flow field; no shroud; solids; vertical plane.
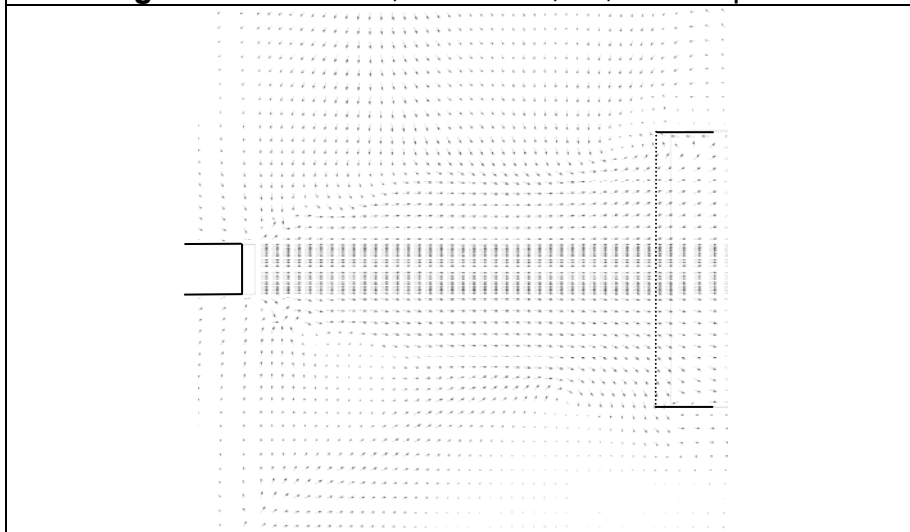
Figure 9. Flow field; no shroud; air; horizontal plane.
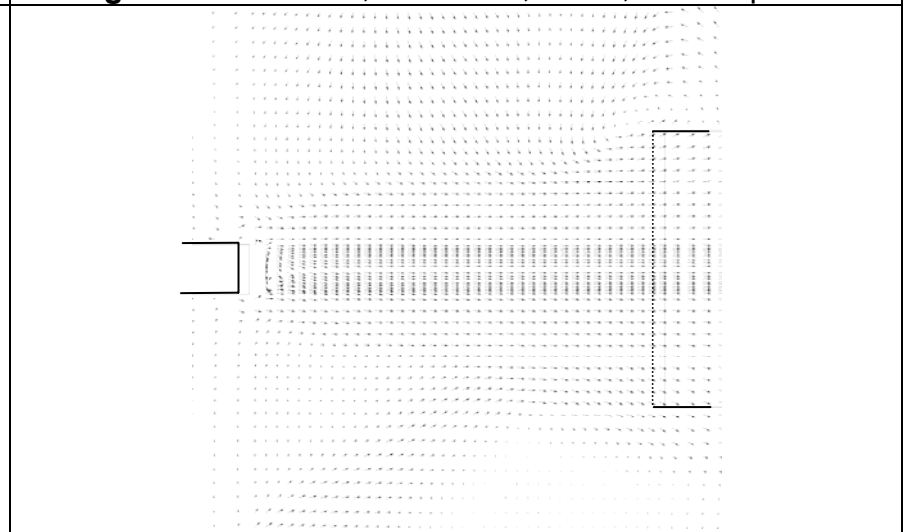
Figure 10. Flow field; no shroud; solids; horizontal plane.
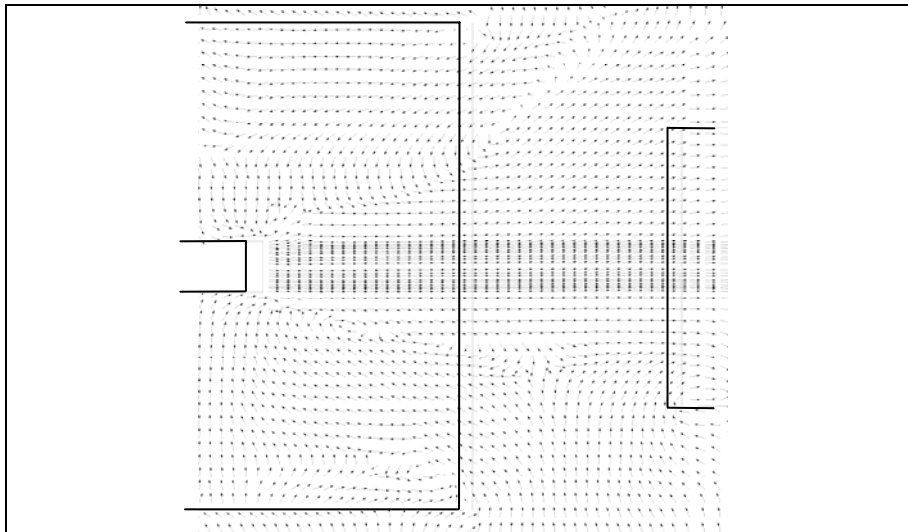
Figure 11. Flow field; shroud; air; vertical plane.
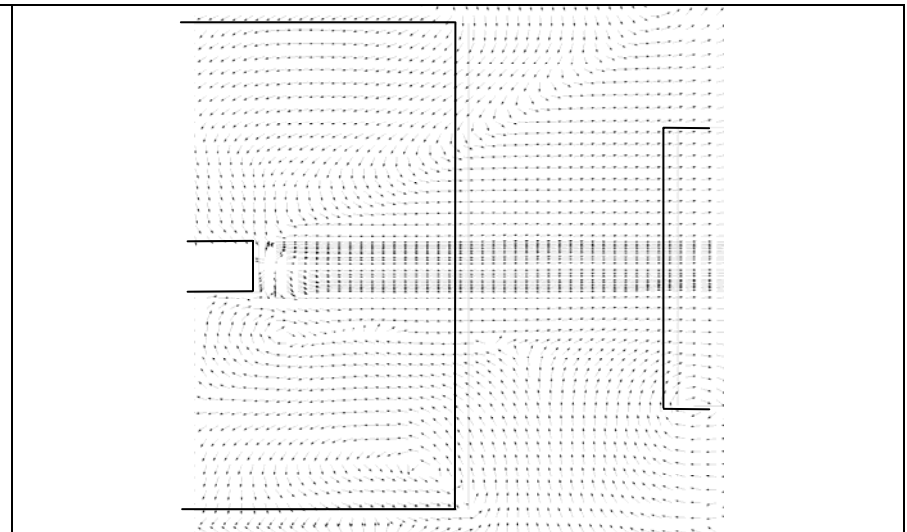
Figure 12. Flow field; shroud; solids; vertical plane.
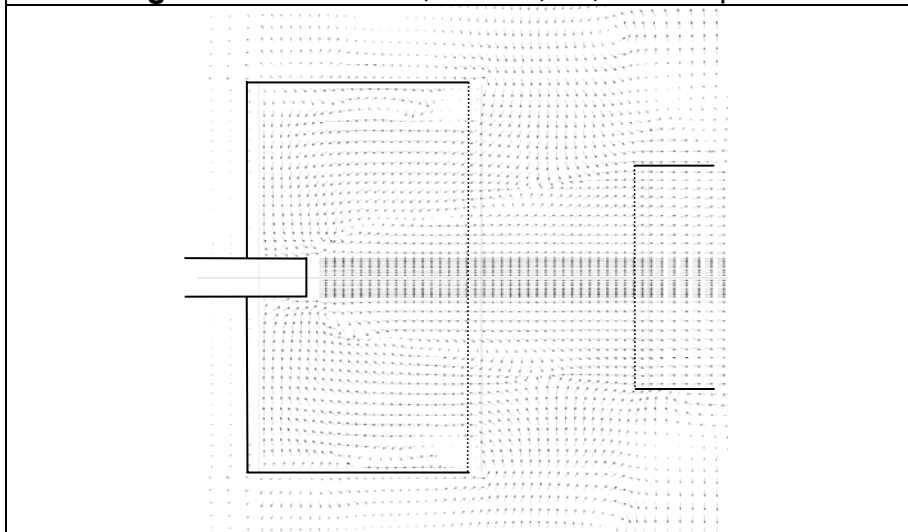
Figure 13. Flow field; shroud; air; horizontal plane.
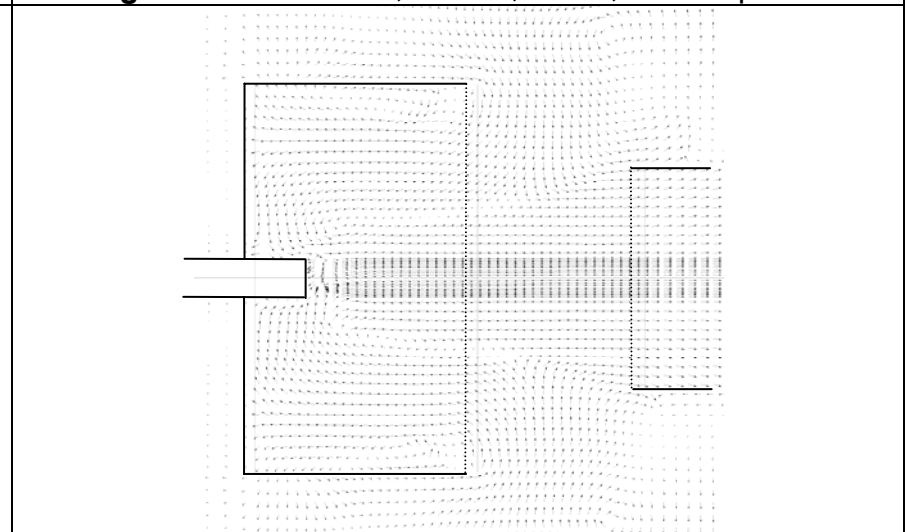
Figure 14. Flow field; shroud; solids; horizontal plane.
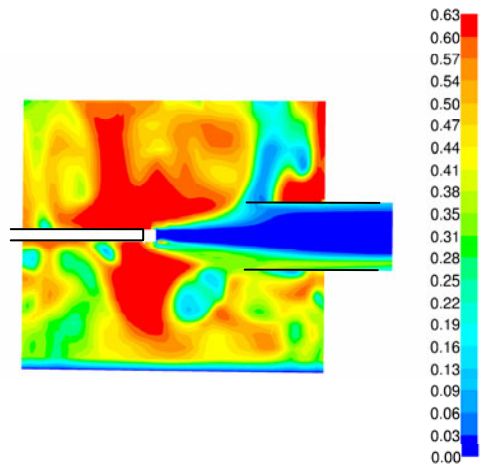
Figure 15. Solids holdup; no shroud; vertical plane.
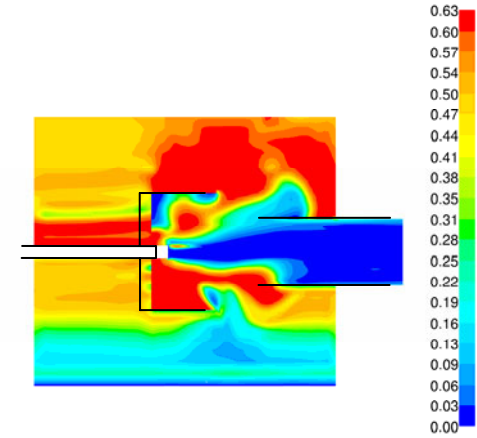
Figure 16. Solids holdup; shroud; vertical plane.
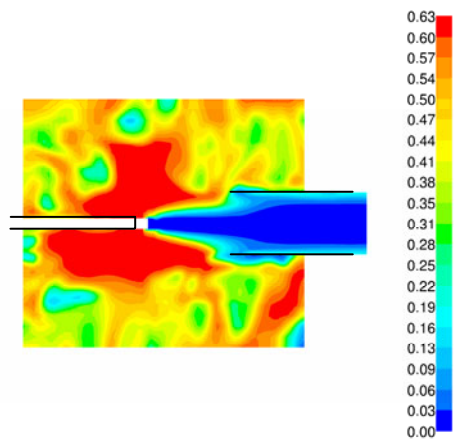
Figure 17. Solids holdup; no shroud; horizontal plane.
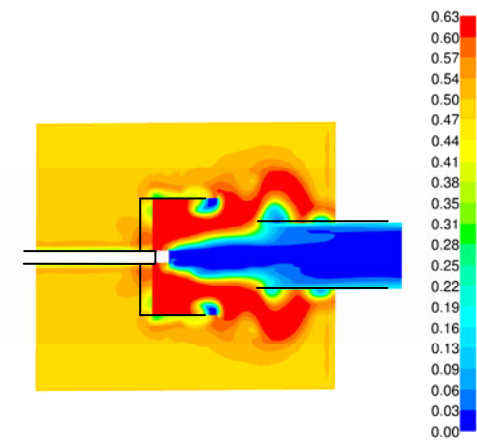
Figure 18. Solids holdup; shroud; horizontal plane.

shroud inlet. Further evidence of this is given by Hulet et al. (2006a) who used a CO_2 tracer and measured a 50% decrease in the volumetric flow rate of gas entrained into the draft tube when a shroud was used then when one was not in place (corresponding to case 1 and case 2). It is also interesting to note from the above figures some more general behaviour of the gas and solids. When no shroud is present, the gas and solids move primarily towards the inlet to the draft tube (see Figures 7 through 10). However, when the shroud is present a large portion of the gas and solids may be observed moving countercurrent to the jet (see Figures 11 through 14). This was also clearly observed in video footage compiled by Hulet et al. (2006b). These two associations, combined with the relatively good agreement between the measured and simulated values for the solids entrainment rate, provide good validation of the CFD simulations.

Figures 15 through 18, which illustrate the solids holdup, provide some insight as to the jet expansion angle. If one were to assume a jet expansion half angle of exactly 12° the jet would enter the draft tube inlet. However, as observed experimentally (Hulet et al., 2003; Ariyapadi et al., 2003) the jet expansion angle is not constant and may vary anywhere between 10 and 15°. Under these circumstances, it would be expected that the jet would be partially overshooting draft tube inlet as may be observed in the aforementioned figures. Another important observation is the fact that the solids holdup encompasses virtually the entire possible range from ~0% to the maximum packing limit. As stated in the introduction, no one drag force model proves accurate over the entire range (Kandhai et al., 2003; Yang et al., 2003). In order to get the most accurate results, it would be desirable to implement more than one drag force model within a given simulation. Unfortunately, it is not currently possible to perform this automatically in FLUENT: to apply more than one drag force model would require a UDF, which would be difficult to implement and very computationally expensive.

Conclusions

Numerical simulations of particle entrainment into a submerged gas jet in a fluidized bed have been carried out using the commercially available CFD software FLUENT (version 6.2.16). The primary objective of this study was to investigate and gain insight into the gas-particle interaction and how the shroud affected the system hydrodynamics, which as the results presented indicate, does have a strong influence on the solids entrainment rate. Relatively strong recirculation zones of the gas phase were observed to form near the mouth of the shroud inlet; however, they were relatively weaker for the solid phase. This also supports previous findings from the authors using CO_2 tracers that indicated a decreased entrainment rate of fluidization gas into the draft tube when a shroud was present. The results presented have been further validated by comparison to experimentally obtained solids entrainment rates and video studies conducted separately (see Hulet et al., 2006a/b).

Acknowledgements

Notation

A	constant in Equation 23
B	constant in Equation 24
C_μ	empirical constant in Equation 5
$C_{1\varepsilon}$	constant in the standard and RNG κ-ε models
$C_{2\varepsilon}$	constant in the standard and RNG κ-ε models
d	nozzle outlet diameter, m
d_p	particle diameter, m
D	draft tube diameter, m
D_H	hydraulic diameter, m
e_{ss}	coefficient of restitution
f	friction coefficient
F_g	gas mass flow rate at the nozzle tip, kg/s
F_s	flow rate of solids exiting the draft tube, kg/s
$\vec{F}_q$	any external body force, N
g	gravitational acceleration constant, m/s^2
$g_{0,ss}$	solid radial distribution function
H_{bed}	fluidized bed height, m
H*	computation domain width, m
K	interphase exchange coefficient
l	distance between the nozzle tip and the draft tube inlet, m
L	draft tube length, m
L*	computational domain length, m
M1/M2/M3	coarse/medium/fine mesh designations
n	total number of phases
N_{Ar}	Archimedes number
N_{Re_t}	Reynolds number for multiparticle terminal setting velocity
$N_{Re_{ts}}$	Reynolds number for single terminal setting velocity
P	pressure, Pa
P'	constant in Equation 24
Q	constant in Equation 24
$\vec{R}_{pq}$	gas-solid interphase exchange coefficient
t	time, s
u	x-axis velocity component, m/s
$v_{r,s}$	terminal velocity correlation parameter
W*	computation domain width, m
x	x-coordinate, m

Greek Letters

α	phase volume fraction
α_κ	constant in the RNG κ-ε model
α_ε	constant in the RNG κ-ε model
$\alpha_{s,max}$	maximum solids packing volume fraction
γ	ratio of specific heats

$\Delta T1/\Delta T2/\Delta T3$ largest/middle/smallest time step size, s

ε turbulent kinetic energy dissipation rate, m^2/s^2

η effectiveness factor

κ turbulent kinetic energy, m^2/s^2

κ_{Θ_s} diffusion coefficient

λ bulk viscosity, kg/m.s

μ shear viscosity, kg/m.s

$\vec{v}$ phase velocity vector, m/s

Θ_s granular temperature, m^2/s^2

ρ phase density, kg/m^3

σ_κ constant in the standard κ-ε model

σ_ε constant in the standard κ-ε model

$\overline{\overline{\tau}}$ Reynolds stress tensor, Pa

τ_s particle relaxation time, s

ϕ_{ls} energy exchange term between the lth fluid phase and the sth solid phase

Subscripts

col   collisional

e/eff   effective

g   gas phase

i   generic phase

j   generic phase

k   generic phase

kin   kinetic

l   laminar

p   secondary phase

q   primary phase

s   solid (particulate) phase

T   turbulent

References

1. Chan, E.W., S. McDougall, and B. Knapper. "Nozzle/mixer assembly", United States Patent (2006): 7,025,874.
2. Cui, M., A.G. Straatman, and C. Zhang. "A computation study of gas-solid flow in an enhanced solid entrainment nozzle system." IJCRE 3 (2005): A7.
3. DallaValle, J.M. Micromeritics, the technology of fine particles. New York: Pitman Publishing Corp., 1948.
4. Ding, J. and D. Gidaspow. "A bubbling fluidization model using kinetic theory of granular flow." AIChE Journal 36.4 (1990): 523 – 538.
5. Du, W., X. Bao, J. Xu, and W. Wei. "Computational fluid dynamics (CFD) modeling of spouted bed: influence of frictional stress, maximum packing limit, and the coefficient of restitution of particles." Chemical Engineering Science 61 (2006a): 4558 – 4570.
6. Du, W., X. Bao, J. Xu, and W. Wei. "Computational fluid dynamics (CFD) modeling of spouted bed: assessment of drag coefficient correlations." Chemical Engineering Science 61 (2006b): 1401 – 1420.

7. Felli, V. <u>Solids entrainment from a fluidized bed into a gas-liquid jet</u>. MESc Thesis, The University of Western Ontario, 2002.

8. <u>FLUENT User Guide</u>. FLUENT User Services Center, 2005. 14 August 2006. <http://www.fluentusers.com/fluent/doc/ori/html/ug/main_pre.htm>.

9. House, P., M. Saberian, C. Briens, F. Berruti, and E.W. Chan. "Injection of a liquid spray into a fluidized bed: particle-liquid mixing and impact on fluid coker yields." <u>Industrial and Engineering Chemistry Research</u> 43.18 (2004): 5663 – 5669.

10. Hulet, C., C. Briens, F. Berruti, E.W. Chan. "Entrainment and stability of a horizontal gas-liquid jet in a fluidized bed." <u>IJCRE</u> 1 (2003): A60.

11. Hulet, C., C. Briens, F. Berruti, E.W. Chan. "Effect of a shroud on entrainment into a submerged jet within a fluidized bed." Unpublished (pending patent application and review/approval by Syncrude Canada Ltd.), 2006a.

12. Hulet, C., C. Briens, F. Berruti, E.W. Chan. "Visualization of the effect of a shroud on entrainment of fluidized solids into a gas jet." Unpublished (pending patent application and review/approval by Syncrude Canada Ltd.), 2006b.

13. Kandhai, D., J.J. Derksen, and H.E.A. Van den Akker. "Interphase drag coefficients in gas-solid flows." AIChE Journal 49.4 (2003): 1060 – 1065.

14. Lun, C.K.K., S.B. Savage, D.J. Jeffrey, and N. Chepurniy. "Kinetic theories for granular flow: inelastic particles in Couette flow and slightly inelastic particles in a general flowfield." J. Fluid Mech. 140 (1984): 223 – 256.

15. Makkawi, Y. and R. Ocone. "Modelling the particle stress at the dilute-intermediate-dense flow regimes: a review." KONA 23 (2005): 49 – 63.

16. Ogawa, S., A. Umemura, and N. Oshima. "On the equations of fully fluidized granular materials." <u>J. of Applied Mathematics and Physics (ZAMP)</u> 31 (1980): 483 – 493.

17. Slater, J.W. "Examining spatial (grid) convergence." NPARC Alliance CFD Verification and Validation Web Site. 13 August 2006 <http://www.grc.nasa.gov/WWW/wind/valid/tutorial/spatconv.html>.

18. Syamlal, M., W. Rogers, T.J. O'Brien. <u>MFIX Documentation Theory Guide: Technical Note</u>. Morgantown: U.S. Department of Energy, 1993. 11 August 2006 <http://www.mfix.org/documentation/Theory.pdf>.

19. Syamlal, M. and T.J. O'Brien. "Computer simulation of bubbles in a fluidized bed." <u>AIChE Symposium Series</u> 270.85 (1985): 22 – 31.

20. Syamlal, M. and T.J. O'Brien. "Fluid dynamic simulation of O_3 decomposition in a bubbling fluidized bed." AIChE Journal 49.11 (2003): 2793 – 2801.

21. Taghipour, F. N. Ellis, and C. Wong. "CFD modeling of a two-dimensional fluidized bed reactor." <u>Proceedings of the 11th Annual Conference of the CFD Society of Canada</u>, 2003. 11 August 2006 <http://tetra.mech.ubc.ca/CFD03/papers/paper29AF3.pdf>.

22. Tu, J.Y. and C.A.J. Fletcher. "Numerical computation of turbulent gas-solid particle flow in a 90° bend. AIChE Journal 41.10 (1995): 2187 – 2197.

23. Tyler, J. and P. Mees. "Using CFD to model the interaction of a horizontal feed jet on fluidized bed hydrodynamics." <u>Second International Conference on CFD in the Minerals and Process Industries</u>, 1999. 11 August 2006 <http://www.cfd.com.au/cfd_conf99/papers/027TYLE.PDF>.

24. Van Wachem, B.G.M., J.C. Schouten, C.M. van den Bleek, R. Krishna, and J.L. Sinclair. "Comparitive analysis of CFD models of dense gas-solid systems." <u>AIChE Journal</u> 47.5 (2001): 1035 – 1051.

25. Van Wachem, B.G.M., J.C. Schouten, R. Krishna and C.M. van den Bleek. "Eulerian simulations of bubbling behaviour in gas-solid fluidised beds." Computers Chem. Engng. 22 (1998): S299 – S306.
26. Van Wachem, B.G.M., J.C. Schouten, R. Krishna and C.M. van den Bleek. "Validation of the Eulerian simulated dynamic behaviour of gas-solid fluidised beds." Chemical Engineering Science 54 (1999): 2141 – 2149.
27. Yang, N., W. Wang, W. Ge, and J. Li. "CFD simulation of concurrent-up gas-solid flow in circulating fluidized beds with structure-dependent drag coefficient." Chemical Engineering Journal 96 (2003): 71 – 80.
28. Zhang, K., J. Zhang, and B. Zhang. "CFD simulation of jet behaviour and voidage profile in a gas-solid fluidized bed." Int. J. Energy Res. 28 (2004): 1065 – 1074.
29. Zimmermann, S. and F. Taghipour. "CFD modeling of the hydrodynamics and reaction kinetics of FCC fluidized-bed reactors." Ind. Eng. Chem. Res. 44 (2005): 9818 – 9827.